AIAA JOURNAL
Vol. 62, No. 3, March 2024

Free Vibration of a Panel Supported by a Shear Compliant Two-Flexure Hinge

B. Yasara Dharmadasa*
University of Colorado, Boulder, CO 80303
Juan Mejia-Ariza,† Jonathan Sauder,‡ Paolo Focardi,§ and Samuel Case Bradford¶
Jet Propulsion Laboratory, California Institute of Technology, Pasadena, CA 91109
Manan Arya**
Stanford University, Stanford, CA 94305
and
Francisco López Jiménez††
University of Colorado, Boulder, CO 80303

https://doi.org/10.2514/1.J063165

Elastically deformable hinges or deployable booms commonly follow architectures with face-skin layers only, cutting out the core to facilitate folding. This significantly reduces the shear stiffness of the hinge, which might reduce the first resonance frequency of the structure. We rationalize the free vibration of the system and the interplay between shearing and bending deformation by deriving an analytical formulation using Timoshenko's beam theory. The framework is derived for a general beam and applied to a case of two flexures of arbitrary geometry with no core. Investigating the specific geometry of flat flexures reveals the existence of two nondimensional length ratios that capture the interplay between inertia, bending stiffness, and shear stiffness of the hinge. Our model explains the dependence of the frequency on the parameters of the system, as well as the dimensions that determine the transition between bending- and shear-dominated vibration modes. Comparison with finite element simulations shows that our analytic framework is able to predict the first natural frequency with less than 1% error. Additionally, an experimental validation was carried out using steel flexures and acrylic panels, showing good agreement with the predictions.

Nomenclature

A	=	axial stiffness of a single flexure, N
a_i	=	distance between the two tape-springs, m
D	=	bending stiffness of a single flexure, N · m^2
D_T	=	bending stiffness of Timoshenko beam, N · m^2
E	=	Young's modulus, N · m^{-2}
$\boldsymbol{F}$	=	force vector
f_i	=	natural frequency for ith mode, Hz
G_T	=	shear stiffness of Timoshenko beam, N
H	=	mode shapes normalized by cantilever beam solution
h	=	flat flexure thickness, m
$\boldsymbol{K}$	=	stiffness matrix
L_h	=	hinge length, m
L_p	=	panel length, m
M	=	bending moment, N · m
$\boldsymbol{M}$	=	mass matrix
m	=	mass of the panel, kg
Q	=	shear force, N · m
R	=	tape-spring radius, m
$R^{\pm}$	=	nondimensional parameter from length scales
t	=	tape-spring thickness, m
t_p	=	panel thickness, m
U_i	=	translation (where i is equal to δ) and rotation (where i is equal to θ) components of the mode shape
v	=	beam deflection, m
v'	=	slope of the beam
W_h	=	hinge width, m
W_p	=	panel width, m
y_c	=	tape-spring neutral axis, m
α, γ	=	reordered terms of $R^{\pm}$ for Taylor expansion
β	=	length ratio equal to $\beta_x\beta_y$
β_x	=	length ratio equal to L_h/L_p
β_y	=	length ratio equal to Δ/h
Δ	=	distance between the neutral axes of two flexures, m
δ	=	panel translation, m
θ	=	angle of panel rotation, rad
ξ	=	bending to shear parameter
φ	=	tape-spring angle, rad
ρ	=	density, kg · m^{-3}
ω	=	angular frequency, rad · s^{-1}

Presented as Paper 2022-0651 at the AIAA SciTech, San Diego, CA, January 3–7, 2022; received 10 May 2023; revision received 26 October 2023; accepted for publication 14 December 2023; published online 13 February 2024.

*Graduate Student, Ann and H.J. Smead Department of Aerospace Engineering Sciences. Student Member AIAA.
†Technologist and Instructor of Advanced Composite Structures, Materials Development, Testing and Failure Investigations Group. Senior Member AIAA.
‡Mechatronics Engineer, Technology Infusion Group. Senior Member AIAA.
§Senior RF Microwave Engineer, Spacecraft Antennas Group.
¶Project Manager, Starshade Technology Development Activity. Associate Fellow AIAA.
**Assistant Professor, Department of Aeronautics and Astronautics. Senior Member AIAA.
††Assistant Professor, Ann and H.J. Smead Department of Aerospace Engineering Sciences; Francisco. LopezJimenez@colorado.edu. Senior Member AIAA (Corresponding Author).

I. Introduction

THE design of space structures is limited by the weight and volume constraints of the launch vehicle and often uses hinges to stow and deploy large elements such as solar panels, radar, telescopes, and antennas [1]. Several designs use mechanical hinges, actuated externally or through rotational springs [2–5]. An alternative is the use of structural elements that can fold elastically without failure. These elements use the strain energy stored during stowage to drive deployment, and reduce parasitic weight and complexities due to friction. Furthermore, they can be built from the same material

as the rest of the structural support (e.g., thin carbon fiber composite laminates), avoiding strains due to mismatch in mechanical and thermal properties.

Several designs for elastically deformable deployable structures use booms made with thin shells that can be flattened and rolled, and whose structural performance (e.g., the relative stiffness under different loadings) can be tuned by controlling the geometry of the cross section [6]; see Fig. 1a. In these architectures, the whole boom is deformed during stowage. Alternatively, it is possible to design structures in which folding is localized in a small region, either by cutting sections out of a thin tube [7,8] (see Fig. 1b) or by bonding two flexible elements [9,10] (see Fig. 1c). The flexible elements allowing folding are usually curved thin shells, such as tape-springs, because they can be flattened and bent to a tight radius while providing high bending stiffness in the deployed state [11–13]. An example of a spacecraft using this architecture is DLR's Eu:CROPIS, where four 0.8 m × 0.8 m solar panels were deployed using glass fiber reinforced polymer tape-spring hinges [14]; see Fig. 1a. Many studies investigate possible extensions of this approach to CubeSat missions [15,16] and precision deployments [13], as well as using novel materials to enhance performance, such as shape memory alloys for controlled release [17,18] or elastomer-based composites for higher compaction [19].

Because they operate in microgravity, the main requirement for deployable space structures is not the response to loading; rather, it is to survive launch accelerations, successfully deploy, and achieve a natural frequency higher than expected excitations to avoid resonance [20]. This last requirement is particularly important for elastically foldable hinges because, by design, they are compliant. However, most of the work on the dynamics of flexure-based hinges has centered on their deployment dynamics [21–26]. There are comparatively fewer studies performing modal analysis, and they usually focus on experimentally or numerically characterizing the first resonance frequency of a single design instead of providing general guidelines [16,17, 27–31]. A general understanding of the design space would be particularly useful for hinges with two thin flexures, such as those shown in Fig. 1, because the absence of a core structure results in significant shear compliance, which can be the driving deformation mode for the first resonance frequency [32].

Flexure systems have been used in vibration testing apparatus as the support platform. However, studies predicting the natural frequencies often ignore the coupling effects between different degrees-of-freedom and vibration modes [33,34]. In particular, the coupling between bending and shear modes of the tape-spring hinges has been previously observed experimentally [25] and therefore needs to be accounted for. This paper addresses this challenge by rationalizing how the material and geometrical parameters of an elastic flexure connected to a rigid panel dictate not only the value of the first resonance frequency but also the interplay between bending- and shear-dominated vibration modes. We assume the response does not change along the width direction, so that the system can be modeled as a two-dimensional (2-D) structure and use Timoshenko's beam theory [35] to account for both bending and shear compliance at the flexible beam. We identify two nondimensional length ratios that govern the response and divide the design space into regions of well-defined and distinct behavior. Furthermore, our closed-form solution for the frequency and vibrational modes allows us to explore different limit cases of the geometry, which we can relate to well-understood systems such as a cantilever beam with a point mass. However, the 2-D simplification restricts the analysis from finding out-of-plane modes, such as torsion, which might be critical for certain designs. This study does not consider torsional modes because the out-of-plane deformation can easily be decoupled and solved as a stand-alone problem.

The paper proceeds as follows: first, Sec. II presents our model; then Sec. III provides insight into the influence of each parameter through an in-depth parametric study and analysis of the limit cases. The model is validated in Sec. IV using finite element simulations and experiments. Section V shows that our model can be readily applied to nonflat geometries, and Sec. VI concludes the paper with a discussion of the findings.

II. Derivation of Natural Frequency

This section will describe our modeling framework to rationalize the free vibration of a panel connected to a flexure hinge with both bending and shear compliance. We first present a general formulation valid for any cross section. Later, we will apply it to the specific case of two thin flexures, as shown in Fig. 1.

A. General Solution

We consider a rigid panel with length L_p, width W_p, and thickness t_p, which is attached to a fixed boundary through a flexible hinge of length L_h and width W_h; see Fig. 2a. We consider that the hinge can either bend or shear within the $x - y$ plane, so that we describe the vibration of the panel through two degrees of freedom (DOFs): vertical translation δ and rotation around its point of connection to the hinge θ; see Figs. 2b and 2c. Because we do not consider out-of-plane deformations for the panel, the flexure can be modeled as a Timoshenko beam of bending stiffness D_T and shear stiffness G_T. The panel mass is uniformly distributed with a total value of m. We assume that the mass of the hinge can be neglected.

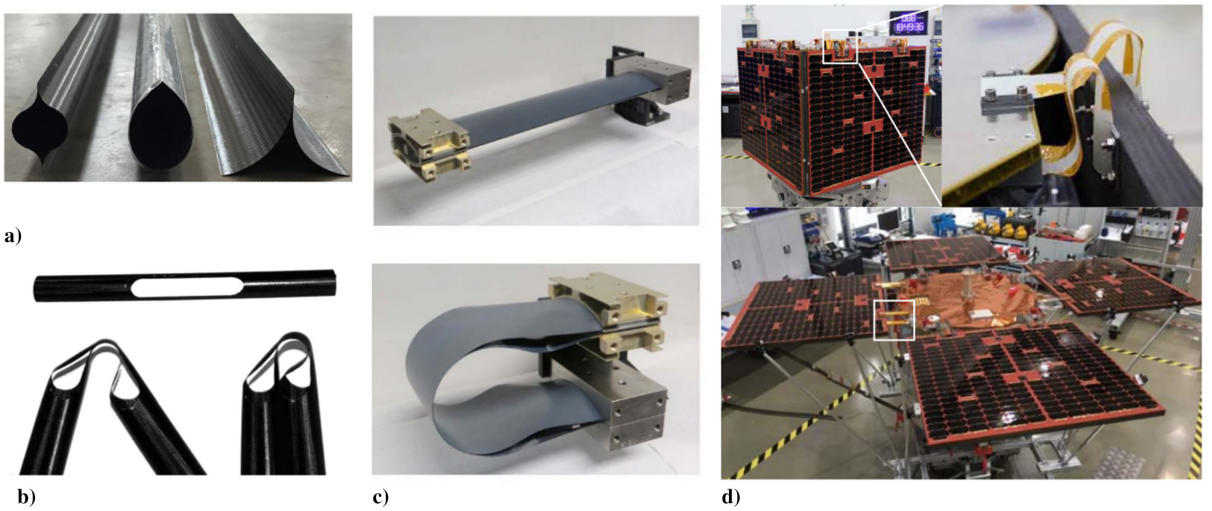

Fig. 1 Flexible deployable booms: a) CTM, SHEARLESS, TRAC [6] (Image: NASA) and b) tape-spring [8] (reprinted with permission from the authors); c) flexure hinge designed for high-precision deployments [10] (reprinted with permission from the authors); d) Eu:CROPIS satellite using tape-spring hinges [14] (image: ESA).

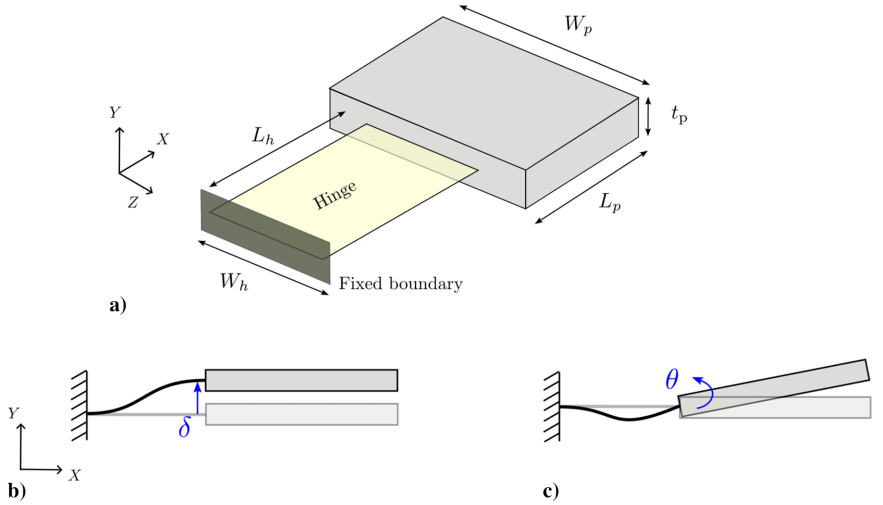

Fig. 2 a) Rigid panel connected to a flexure hinge. Degrees of freedom considered in $x-y$ plane: b) translation δ and c) rotation θ.

We write the two-degree-of-freedom equation of motion for this system as

$$\boldsymbol{M}\ddot{\boldsymbol{x}} + \boldsymbol{K}\boldsymbol{x} = \boldsymbol{F} \tag{1}$$

where the DOFs are $\boldsymbol{x} = [\delta, \theta]^T$, the applied forces are $\boldsymbol{F} = [F_\delta, M_\theta]^T$, and the stiffness matrix is

$$\boldsymbol{K} = \begin{bmatrix} K_{\delta\delta} & K_{\delta\theta} \\ K_{\theta\delta} & K_{\theta\theta} \end{bmatrix} \tag{2}$$

and the mass matrix is

$$\boldsymbol{M} = \begin{bmatrix} m_{\delta\delta} & m_{\delta\theta} \\ m_{\theta\delta} & m_{\theta\theta} \end{bmatrix} \tag{3}$$

1. *Stiffness Matrix*

The hinge is subjected to force F_1 and moment M_1 as reactions at the fixed boundary, and to force F_2 and moment M_2 at the connection with the panel; see Fig. 3a. The vertical deflection of the neutral axis of the hinge is $v(x)$. The components of the stiffness matrix are the values of F_2 and M_2 required to induce a unit value of each of the two degrees of freedom, which are equal to the value of the displacement and rotation of the hinge at the end, $\delta = v(L_h)$ and $\theta = v'(L_h)$, respectively.

Following Timoshenko's beam theory, we assume that plane sections remain plane while not necessarily perpendicular to the neutral axis due to shear deformation [35]. Shear strain is assumed to be constant along the hinge length. We consider small deformations and linear elasticity. The slope of the beam deflection can then be calculated as

$$v'(x) = -\frac{Q(x)}{G_T} + \int_0^x \frac{M(s)}{D_T}\mathrm{d}s \tag{4}$$

where s is a dummy variable with $M(s)$ being the internal bending moment at a point s and $Q(x)$ is the internal shear force at a point x; see Fig. 3b.

We integrate Eq. (4) to obtain $v(x)$, with boundary conditions $v(0) = v'(0) = 0$ at the clamped end and two possible sets of boundary conditions at the other end: $\delta = v(L_h) = 1$ and $\theta = v'(L_h) = 0$, or $\delta = v(L_h) = 0$ and $\theta = v'(L_h) = 1$; see Figs. 3c and 3d. This results in the values of F_2 and M_2 necessary to build the stiffness matrix:

$$\boldsymbol{K} = \begin{bmatrix} F_{2,\delta=1,\theta=0} & M_{2,\delta=1,\theta=0} \\ F_{2,\delta=0,\theta=1} & M_{2,\delta=0,\theta=1} \end{bmatrix} = \begin{bmatrix} \dfrac{12D_T}{L_h^3\xi} & \dfrac{-6D_T}{L_h^2\xi} \\ \dfrac{-6D_T}{L_h^2\xi} & \dfrac{4D_T(3D_T + G_T L_h^2)}{G_T L_h^3 \xi} \end{bmatrix} \tag{5}$$

where $\xi = ((12D_T/G_T L_h^2) + 1)$ is a nondimensional parameter indicating the ratio of bending stiffness versus shear stiffness. We

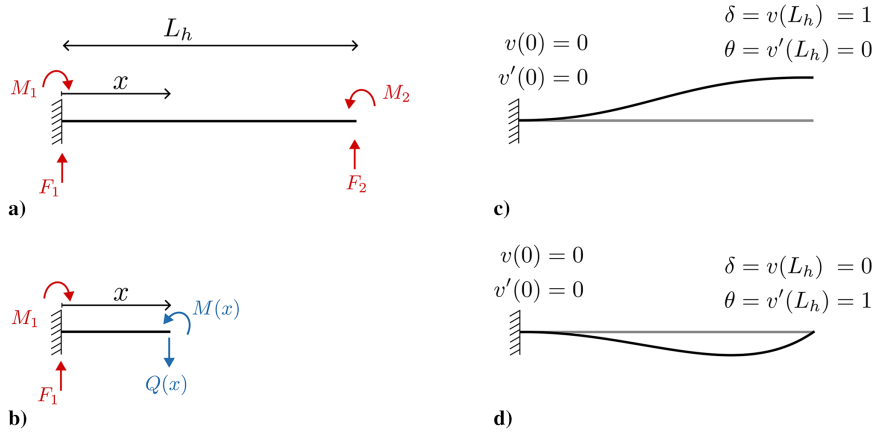

Fig. 3 Free body diagram for a) external loads on the hinge and b) internal bending moment and shear force; c-d) schematics of the hinge and boundary conditions used to calculate the stiffness terms.

can recover the Euler–Bernoulli case (no shear deformation) by taking the limit of $G_T \to \infty$, which results in $\xi = 1$.

2. Mass Matrix

The mass matrix $\boldsymbol{M}$ is obtained by calculating the reaction force and moment for unit accelerations in pure translation ($\ddot{\delta} = 1, \ddot{\theta} = 0$) and pure rotation ($\ddot{\delta} = 0, \ddot{\theta} = 1$) of the panel. Figure 4 shows the inertia forces and moments for each case if the DOFs are defined at the center of the mass of the panel (in blue) and at the panel edge transferring to the beam (in black). Note that the translation and rotation terms are coupled for the two modes. For example, a unit acceleration in the translational DOF would impose a force of $m\ddot{\delta}$ and no moment if the DOF was defined at the center of the mass. In our case, because the DOFs are defined at the end of the panel, achieving the same acceleration requires the same force and an additional moment of $m\ddot{\delta}L_p/2$ to maintain $\ddot{\theta} = 0$. The resulting mass matrix is therefore non-diagonal:

$$\boldsymbol{M} = \begin{bmatrix} m & \frac{mL_p}{2} \\ \frac{mL_p}{2} & \frac{mL_p^2}{3} \end{bmatrix} \tag{6}$$

3. Free Vibration of the System

For free vibration, we solve the equation of motion, Eq. (1), with $\boldsymbol{F} = [0, 0]^T$ and $\boldsymbol{x} = [u_\delta, u_\theta]^T e^{i\omega t}$. Substituting the mass and stiffness matrix we obtain the following:

$$\begin{bmatrix} -m\omega^2 + \frac{12D_T}{L_h^3\xi} & -\frac{mL_p}{2}\omega^2 - \frac{6D_T}{L_h^2\xi} \\ -\frac{mL_p}{2}\omega^2 - \frac{6D_T}{L_h^2\xi} & -\frac{mL_p^2}{3}\omega^2 + \frac{4D_T(3D_T + G_T L_h^2)}{G_T L_h^3 \xi} \end{bmatrix} \begin{bmatrix} u_\delta \\ u_\theta \end{bmatrix} = \begin{bmatrix} 0 \\ 0 \end{bmatrix} \tag{7}$$

Equation (7) has a nontrivial solution when the matrix is singular, so we find the resonant frequencies by making the determinant equal to zero, which yields

$$f_1 = \frac{1}{2\pi}\sqrt{\frac{12D_T R^-}{mL_h^3\xi}} \quad f_2 = \frac{1}{2\pi}\sqrt{\frac{12D_T R^+}{mL_h^3\xi}} \tag{8}$$

with mode shapes

$$\begin{bmatrix} \frac{U_\delta}{L_h} \\ U_\theta \end{bmatrix}_1 = \begin{bmatrix} \frac{1}{2}\left(1 + \frac{L_p}{L_h}R^-\right) \\ (1 - R^-) \end{bmatrix} \quad \begin{bmatrix} \frac{U_\delta}{L_h} \\ U_\theta \end{bmatrix}_2 = \begin{bmatrix} \frac{1}{2}\left(1 + \frac{L_p}{L_h}R^+\right) \\ (1 - R^+) \end{bmatrix} \tag{9}$$

where the translation is scaled by the hinge length and the subscripts indicate the first and second mode. The difference between the modes is defined by the parameter

$$R^\pm = \left(2 + \frac{(3+\xi)}{2}\frac{L_h^2}{L_p^2} + \frac{3L_h}{L_p}\right) \pm \sqrt{\left(2 + \frac{(3+\xi)}{2}\frac{L_h^2}{L_p^2} + \frac{3L_h}{L_p}\right)^2 - \xi\frac{L_h^2}{L_p^2}} \tag{10}$$

which is a function of the ratio of panel and hinge length, L_h/L_p, respectively, and the nondimensional parameter ξ.

B. Hinge with Two Flexures

Next, we focus on a specialized case of a hinge consisting of two thin flexures where the neutral axes are separated by a distance Δ. This can be idealized as a beam with two flanges and no web or core and captures the behavior of the examples shown in Figs. 1b and 1c. We assume each of the individual layers behaves as a Euler–Bernoulli beam, and the lack of core material results in a significant reduction of the hinge's shear stiffness. Let the axial and bending stiffness of each layer be A and D, respectively. The hinge bending stiffness D_T is calculated using the parallel axis theorem:

$$D_T = 2D\left(1 + \frac{A\Delta^2}{4D}\right) \tag{11}$$

To obtain the shear stiffness G_T, we impose a pure translation motion of $\delta = 1$ and $\theta = 0$ and allow the two flexures to deform independently. The fixed-end moments/forces can be calculated for the Timoshenko hinge by solving Eq. (4), which yields

$$F_T = \frac{12D_T}{L_h^3\xi} \quad M_T = \frac{-6D_T}{L_h^2\xi} \tag{12}$$

The same end forces/moments can be calculated by considering the individual fixed-end moments for the Euler–Bernoulli beam, as shown in Fig 5. Equating either the moment or the force will result in the shear stiffness for the hinge:

$$F_T = \frac{12D_T}{L_h^3\xi} = 2\frac{12D}{L_h^3} \quad M_T = \frac{-6D_T}{L_h^2\xi} = 2\frac{6D}{L_h^2} \tag{13}$$

which yield the same relationship, which include the shear stiffness G_T as part of the ratio ξ. We can then obtain an expression for the shear modulus of the hinge as

$$G_T = \frac{96D^2}{L_h^2 A\Delta^2}\left(1 + \frac{A\Delta^2}{4D}\right) \tag{14}$$

It should be noted that the shear stiffness does not depend on the shear modulus of the material because we are treating the hinge as two thin and stiff elements with nothing to enforce shear stiffness, similar to a sandwich panel with no core or an I-beam with no web. Shear deformation of the hinge therefore corresponds to bending of the two flexures with respect to their respective neutral surfaces, and not with respect to the neutral surface of the hinge. The expression for the shear stiffness in Eq. (14) is therefore very different from the usual treatment in derivations using Timoshenko beam theory [35].

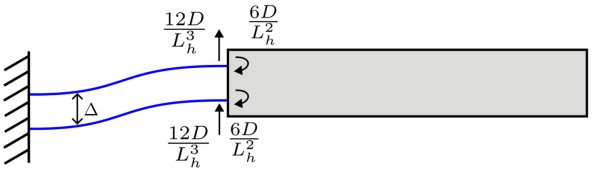

Fig. 5 Estimation of shear modulus for two flexures by imposing a pure shear deformation of $\delta = 1, \theta = 0$.

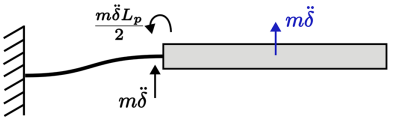

a)

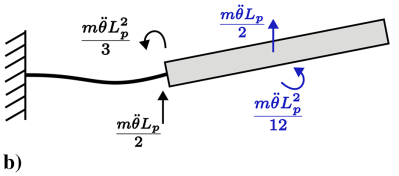

b)

Fig. 4 Inertia terms for the a) translation and b) rotation degree of freedom. Blue color is at panel center and black color is at hinge connection point.

Using the results from Eqs. (11) and (14), we can also rewrite the nondimensional ratio ξ as the following:

$$\xi = 1 + \frac{A\Delta^2}{4D} \tag{15}$$

and the two natural frequencies as

$$f_1 = \frac{1}{2\pi}\sqrt{\frac{24DR^-}{mL_h^3}} \quad f_2 = \frac{1}{2\pi}\sqrt{\frac{24DR^+}{mL_h^3}} \tag{16}$$

Equations (15) and (16) are valid for a hinge design with flexures of arbitrary cross section, including tape-springs and other transversely curved elements. They can also be used to model designs in which flexures are staggered across the width to avoid collision during stowage, as long as there is an equal number of flexures on each side [14].

C. Hinge with Two Flat Flexures

We can further specialize the analysis when the two flexures are flat. If plane stress Young's modulus of the material is E, then the bending and axial stiffness of each flexure can be expressed as

$$D = \frac{1}{12}EW_h h^3 \quad A = EW_h h \tag{17}$$

where W_h is the width of the flexures, which can be, in principle, different than the width of the panel, W_p.

The rest of the terms simplify as

$$D_T = \frac{EW_h h^3}{6}\left(1 + \frac{3\Delta^2}{h^2}\right) \tag{18}$$

$$G_T = \frac{2EW_h h^5}{3L_h^2\Delta^2}\left(1 + \frac{3\Delta^2}{h^2}\right) \tag{19}$$

$$\xi = 1 + \frac{3\Delta^2}{h^2} \tag{20}$$

The two natural frequencies can therefore be expressed as

$$f_1 = \frac{1}{2\pi}\sqrt{\frac{2EW_h h^3 R^-}{mL_h^3}} \quad f_2 = \frac{1}{2\pi}\sqrt{\frac{2EW_h h^3 R^+}{mL_h^3}} \tag{21}$$

In this case, ξ depends only on the geometry of the hinge, and the only stiffness term is E, which does not play a role in the parameter $R^{\pm}$. As a result, the vibrational modes are entirely determined by simple geometric relationships, which will be explored in detail in the following section.

III. Parametric Study

In this section, we study the dependence of each of the parameters on the natural frequency of the system for the case of two flat flexures at a distance Δ. We will particularly focus on obtaining a description of possible scalings and identifying limit cases.

We start with Eq. (21), in which the dependence on Young's modulus E, flexure width W_h, and panel mass m can easily be identified as

$$f \propto \sqrt{\frac{EW_h}{m}} \tag{22}$$

However, the dependence of the rest of the parameters (Δ, h, L_p, and L_h) is more complex because they appear multiple times within $R^{\pm}$ and ξ. To illustrate the complexity of the dependencies, we plot the two natural frequencies as a function of each of the parameters (see Fig. 6), considering variations with respect to a point design with $\Delta = 10$ mm, $h = 0.1$ mm, $L_h = 10$ mm, $L_p = 100$ mm, $m = 1$ kg, $W_h = 100$ mm, and $E = 10$ MPa, marked with a star on each plot. We observe increasing thickness h increases the first natural

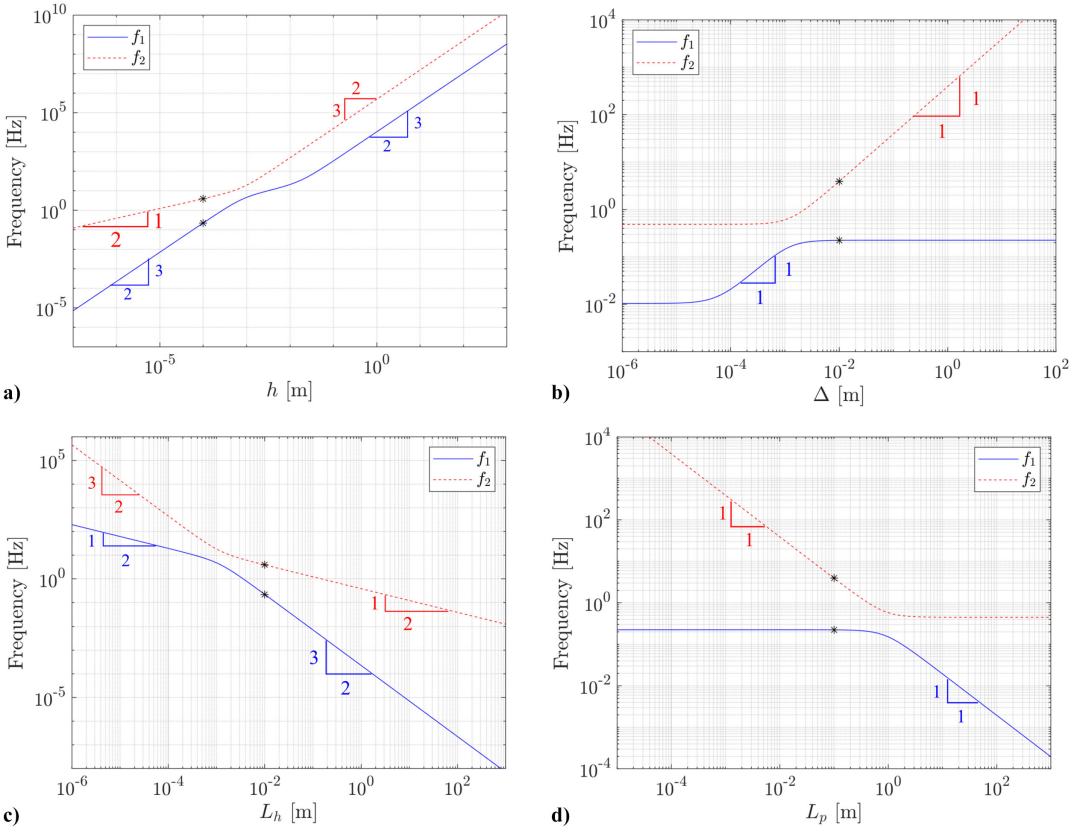

Fig. 6 Frequencies for mode 1 and mode 2 as a function of a) h, b) Δ, c) L_p, and d) L_h. Each parameter was varied while keeping others fixed at the point design (marked by a star on each plot).

frequency at a rate of $f_1 \propto h^{1.5}$ with a slight dip in the 1–10 mm range. On the other hand, increasing Δ does not increase the natural frequency for the first mode. However, decreasing Δ drops the frequency from 0.2 Hz to 0.01 Hz and again saturates to a constant value. Similarly, we observe different power law relations for L_p and L_h with transitions in the behavior at different values. Further exploration of the behavior not presented here shows that the transition points move as the point design values are changed. Although we can explain some of the observed behavior intuitively (e.g., increasing the value of Δ does not affect the first mode once it is dominated by shear deformation), their exact power law and nonlinearity are not clear. Understanding the nonlinear coupling behavior of these parameters is important for design and performance optimization of the hinge. For example, we can retain similar frequency performance even if the panel length is increased to 1 m or the flexure gap Δ is decreased to around 0.001 m. It is important to mention that the results shown in Fig. 6 aim to be an exploration of the parameter space, which might not align with a realistic design for a deployable structure. For example, cases with $\Delta \geq L_h$ would not be able to be folded like the structures in Fig. 1. Our model is able to accurately capture the first vibrational mode even for such geometries, as shown by comparison to finite element simulations in which the flexures are modeled independently; see Sec. IV.C.1.

The nonlinear behavior in Eq. (21) is a result of the $R^{\pm}$ term. To rationalize it, we define the length ratios $\beta_x = (L_h/L_p)$ and $\beta_y = (\Delta/h)$ and their product as $\beta = \beta_x\beta_y$. Doing so, we can rewrite Eq. (10) as

$$R^{\pm} = \left(2 + 3\beta_x + 2\beta_x^2 + \frac{3}{2}\beta_x^2\beta_y^2\right) \times \left(1 \pm \sqrt{1 - \frac{(1+3\beta_y^2)\beta_x^2}{\left(2 + 3\beta_x + 2\beta_x^2 + \frac{3}{2}\beta_x^2\beta_y^2\right)^2}}\right) \tag{23}$$

Figure 7a shows the values of $R^{\pm}$ obtained for different combinations of β_x and β_y, but plotted as a function of β. Each color corresponds to a different quadrant in the $\beta_x - \beta_y$ plane; see Fig. 7b. For additional clarity, we plot dashed lines corresponding to $\beta_x = \{0.1, 1, 10\}$ in blue and $\beta_y = \{0.1, 1, 10\}$ in red. The representative shapes for the evolution of $R^{\pm}$ for the case constant β_y (blue) and constant β_x (red) are sketched in Fig. 7c. The red lines scale linearly in the log scale with increasing β and saturate after a transition point (β_1). The second mode shows the opposite behavior: it starts off at a constant value that later transfers to a linear dependence at the same transition point. The blue curve, which represents a constant β_x, initially starts at a constant value R_1^-, shifts to a log-linear behavior at β_2, and then again saturates after the transition point. The second mode has only a single transition at β_3.

To understand the different regimes and the corresponding transition points, we can further simplify Eq. (23), which is in the form of $R^{\pm} = \alpha(1 \pm (1-\gamma)^{\frac{1}{2}})$, using the binomial theorem. The higher-order terms of the Taylor expansion can be neglected when $\gamma < 1$, which yields the approximation $(1-\gamma)^{\frac{1}{2}} \approx (1 - (1/2)\gamma)$. Hence we have

$$R^- \approx \frac{\alpha\gamma}{2} = \frac{(1+3\beta_y^2)\beta_x^2}{4 + 6\beta_x + 4\beta_x^2 + 3\beta_x^2\beta_y^2} \tag{24}$$

$$R^+ \approx 2\alpha - \frac{\alpha\gamma}{2} \approx 2\alpha = 4 + 6\beta_x + 4\beta_x^2 + 3\beta_x^2\beta_y^2 \tag{25}$$

We can verify that $0 < \gamma_{\max} < 0.25$ for all possible combinations of β_x and β_y, so that the error for our approximation, $R^{\pm}_{\text{error}} = (|R^{\pm} - R^{\pm}_{\text{approx}}|/R^{\pm})$, is bounded by 6.7% (which is the value of the error when $\gamma = 0.25$). Figure 8 shows the error for values of β_x and β_y in the 0.001 to 1000 range, which shows that the higher values of the error are observed in the quadrant where $\beta_x < 1$ and $\beta_y > 1$.

In order to rationalize the different regimes and transitions within them, we will study the behavior of Eq. (25) in the limit cases associated with the different regions in the β_x, β_y plane.

A. Case I: $\beta_x \ll 1$ & $\beta_y \ll 1$

First, we look at the quadrant where both β_x and β_y are smaller than one, resulting in $\beta \ll 1$ (pink region in Fig. 7). In Eqs. (24) and (25), the terms containing β_x and β_y become negligible compared to the other competing terms and $R^{\pm}$ reduce to

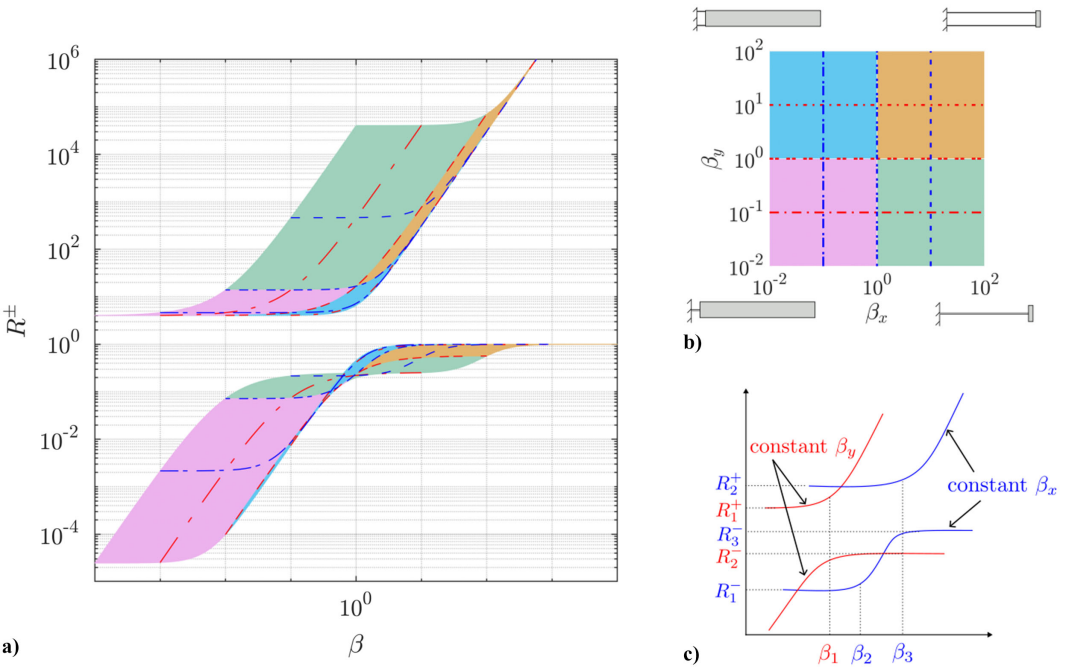

Fig. 7 a) Behavior of $R^{\pm}$ for β_x and β_y in the 0.01 to 100 range, plotted as a function of β; b) color and line coding for corresponding β_x or β_y values; c) characteristic behaviors observed for constant β_x (blue) and constant β_y (red).

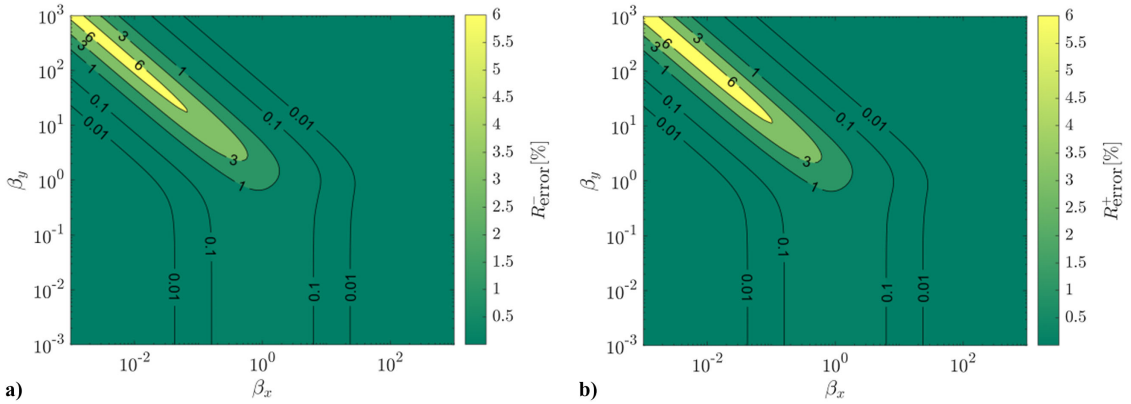

Fig. 8 Approximation error using binomial theorem for a) R^- and b) R^+.

$$R^- \approx \frac{\beta_x^2}{4} \quad R^+ \approx 4 \tag{26}$$

The preceding simplification rationalizes the different behaviors observed when varying β_x versus β_y in Fig. 7c, and the saturation values $R_1^- \approx (\beta_x^2/4)$ and $R_1^+ = R_2^+ \approx 4$. Substituting the above results in Eq. (21), the frequencies can be approximated as

$$f_1 \approx \frac{1}{2\pi}\sqrt{\frac{EW_h h^3}{2mL_p^2 L_h}} \quad f_2 \approx \frac{1}{2\pi}\sqrt{\frac{8EW_h h^3}{mL_h^3}} \tag{27}$$

Physically, this region represents the case of a long panel attached to a very short hinge, and the distance between the flexures is smaller than their thickness (i.e., two flexures with basically no offset that are staggered along the width). In this configuration, the bending to shear parameter is $\xi = 1 + 3\beta_y^2 \approx 1$, and the hinge acts similar to a Euler–Bernoulli beam with twice the width because both flexures are basically equivalent to each other. Hence, Δ does not have any impact on the natural frequency.

B. Case II: $\beta_x \ll 1$ & $\beta_y \gg 1$

Next, we focus on the case where $\beta_y \gg 1$, while the other ratio is still $\beta_x \ll 1$ (blue region in Fig. 7). This again corresponds to a very long panel connected to a short hinge, but now the distance between the flexures is much larger than their thickness, and so the shear stiffness is lower than the bending stiffness ($\xi \gg 1$). Here, we have two possible cases depending on the magnitude of the two length scales, which can be distinguished based on the value of $\beta = \beta_x\beta_y$.

1. *Case II - A ($\beta \ll 1$)*

We first consider the region where $\beta \ll 1$, which implies $(1/\beta_x) \gg \beta_y \gg 1$. In this case, we can consider that contributions from both the β_x and β terms are small, which yields

$$R^- \approx \frac{3\beta_x^2\beta_y^2}{4} \quad R^+ \approx 4 \tag{28}$$

Compared to Case I, only R^- term changes in this region with the transition occurring at $\beta_y = 1$. For the constant β_x curve in Fig. 7c, this transition point corresponds to $\beta = \beta_2 = \beta_x$. The frequencies can then be approximated as

$$f_1 \approx \frac{1}{2\pi}\sqrt{\frac{3EW_h h\Delta^2}{2mL_p^2 L_h}} \quad f_2 \approx \frac{1}{2\pi}\sqrt{\frac{8EW_h h^3}{mL_h^3}} \tag{29}$$

As the flexure spacing is increased, Δ influences the bending stiffness following the parallel axis theorem and appears in the frequency term. However, the second mode does not depend on Δ, suggesting a pure shear deformation mode, which will be verified later by investigating the mode shapes.

2. *Case II - B ($\beta \gg 1$)*

We now consider the case where $\beta \gg 1$, which can be seen as a continuous transition from Case I to Case II-A, so that β_y keeps increasing until $\beta_y \gg (1/\beta_x) \gg 1$. In this case, we only neglect the contribution of β_x, and we obtain

$$R^- \approx \frac{3\beta_x^2\beta_y^2}{3\beta_x^2\beta_y^2} = 1 \quad R^+ \approx 3\beta_x^2\beta_y^2 \tag{30}$$

We observe that both R^- and R^+ terms change, flipping their behavior compared to Case II-A. This transition occurs at $\beta = \beta_3 = 1$ with the saturation value $R_3^- \approx 1$. The frequency terms become

$$f_1 \approx \frac{1}{2\pi}\sqrt{\frac{2EW_h h^3}{mL_h^3}} \quad f_2 \approx \frac{1}{2\pi}\sqrt{\frac{6EW_h h\Delta^2}{mL_p^2 L_h}} \tag{31}$$

As we continue to increase the flexure spacing, the first and second frequency terms flip, with the first mode becoming shear dominated independent of flexure spacing Δ.

C. Case III: $\beta_x \gg 1$ & $\beta_y \ll 1$

Next, we move on to the green quadrant in Fig. 7b, which represents a point mass (i.e., a very short panel) attached to a long Euler–Bernoulli hinge (i.e., hinge separation is smaller than the thickness). Again we have two possible scenarios of $\beta < 1$ and $\beta > 1$, but in both cases only the β_x terms are significant, yielding

$$R^- \approx \frac{\beta_x^2}{6\beta_x + 4\beta_x^2} = \frac{1}{\frac{6}{\beta_x} + 4} \approx 0.25 \quad R^+ \approx 4\beta_x^2 \tag{32}$$

Compared to Case I, R^- and R^+ terms flip their behavior, as apparent from the constant β_y curve. This transition occurs at $\beta_x = 1$ or $\beta = \beta_1 = \beta_y$, and the first mode saturates at $R_2^- \approx 0.25$. The frequency terms become

$$f_1 \approx \frac{1}{2\pi}\sqrt{\frac{EW_h h^3}{2mL_h^3}} \quad f_2 \approx \frac{1}{2\pi}\sqrt{\frac{8EW_h h^3}{mL_p^2 L_h}} \tag{33}$$

Because this case is similar to a cantilever Euler–Bernoulli beam (because $\xi \approx 1$) with a point mass at the tip (because the hinge is much longer than the panel, $L_p \ll L_h$), we can compare our solution to the natural frequency of a beam-concentrated mass system. We consider a beam with twice the width of the flexures, $\text{EI} = (1/12)E(2W_h)h^3$, and the first frequency for a cantilever is the same as the first frequency of our system:

$$f_{\text{cantilever}} = \frac{1}{2\pi}\sqrt{\frac{3\text{EI}}{mL_h^3}} = f_1 \tag{34}$$

D. Case IV: $\beta_x \gg 1$ & $\beta_y \gg 1$

The final quadrant corresponds to the case when both length scales are greater than one. The limit case for this region represents a point mass (hinge longer than the mass) attached to a hinge with high bending stiffness and low shear stiffness ($\xi \gg 1$). In this case, the β terms become significant and we can approximate $R^{\pm}$ as

$$R^- \approx \frac{3\beta_x^2\beta_y^2}{3\beta_x^2\beta_y^2} = 1 \quad R^+ \approx 3\beta_x^2\beta_y^2 \tag{35}$$

This is the same behavior as Case II-A, and therefore the constant β_y lines remain the same. However, constant β_x curves passing through Case III transitions at $\beta_y = 1$ or $\beta = \beta_3 = \beta_y$ in Fig. 7c. The frequency terms are

$$f_1 \approx \frac{1}{2\pi}\sqrt{\frac{2EW_h h^3}{mL_h^3}} \quad f_2 \approx \frac{1}{2\pi}\sqrt{\frac{6EW_h h\Delta^2}{mL_p^2 L_h}} \tag{36}$$

E. Summary of All Cases

We summarize the parameter dependency derived from the preceding analysis in Fig. 9. The dashed lines indicate the transition boundaries. The first vibrational mode has four characteristic behaviors whereas the second mode has three. With this insight, we can go back to the previous example in Fig. 6 and explain the parameter dependence. The red star in Fig. 9 represents the point design case, and the two arrows indicate the four possible parameter sweeping directions: vertical direction for changes in h or Δ, and horizontal direction for changes in L_h or L_p. Upon increasing the thickness h, two transition boundaries are crossed for the first mode, whereas the second mode is met only with a single boundary, as observed in Fig. 6a. For the hinge length L_h, only one transition boundary is crossed for both modes, as observed in Fig. 6c. Similarly, we can explain the behavior of all the parameters, as well as all the slopes reported in Fig. 6 for all possible parameter variations.

F. Vibrational Mode Shapes

In Sec. II, Eq. (9), we derived an analytic equation for the mode shapes that only depends on the hinge geometry. We extend the previous analysis to obtain some intuition regarding the modes in all the regions of the $\beta_x - \beta_y$ design space and compare it to the behavior expected based on the relative magnitude of the stiffness of the hinge (bending versus shear) and the inertia of the panel (translational versus rotational).

Because the modes are characterized by the ratio between the two components, we define

$$H_i(R^{\pm}) = \frac{U_{\theta,i}}{\tilde{U}_{\delta,i}} \tag{37}$$

where $U_{\theta,i}$ is the rotational component of the ith mode, and $\tilde{U}_{\delta,i} = (3U_{\delta,i}/2L_h)$ is a normalization of the displacement component δ. The prefactor $3/2$ in the normalization corresponds to the ratio of rotation to deflection of a Euler–Bernoulli cantilever beam with a mass at the tip. With this normalization, we expect to recover $H_1 \approx 1$ for the case of a cantilevered beam with point mass ($\beta_x \gg 1$ and $\beta_y \ll 1$), suggesting the mode is independent of the shear stiffness of the beam. This is indeed confirmed in Fig. 10a, where we plot the variation of H_1. When we increase β_y while keeping $\beta_x \gg 1$, we move into a zone of $H_1 \approx 0$. This corresponds to a pure translation mode dependent only on the shear stiffness of the beam. In the region $\beta_x \ll 1$ and $\beta_y \ll 1$, we observe the panel rotation to be significant compared to its translation. For $\beta_x \ll 1$ and $\beta_y \gg 1$, the mode shape is a combination of translation and rotation.

Similarly, we plot the second mode shapes H_2 in Fig. 10b, which shows a surprising dependence only on the inertial term β_x. Furthermore, we observe that the ratio of rotation to translation is equal to either $-\beta_x$ or $-1.33\beta_x$ for all possible scenarios. That is, when the panel inertia is much higher, we should expect larger positive translations compared to smaller negative rotations and vice versa. Although we were able to distinguish the roles of shear and bending stiffness in the first mode, similar insight cannot be claimed for the second mode because the mode shapes are more complicated and likely involve both deformations.

IV. Experimental and Numerical Validation

In this section, we compare and validate the analytic derivations with numerical results from high-fidelity simulations and experiments.

A. Experimental Setup

We prototype a representative hinge geometry using spring steel flexures and acrylic plates. The acrylic is laser cut to be 76.2 mm by 76.2 mm squares. All flexures have the same width of 76.2 mm and the same thickness of 0.127 mm, while the length was varied, as shown in Table 2. The steel flexures are attached to the acrylic plates using through-bolts and nuts; see Fig. 11a. Different hinge geometries are obtained by varying the hinge length (L_h) and the thickness of the core acrylic layer (which changes Δ as well as the panel mass, m). It should be noted that the prototypes are not designed to be

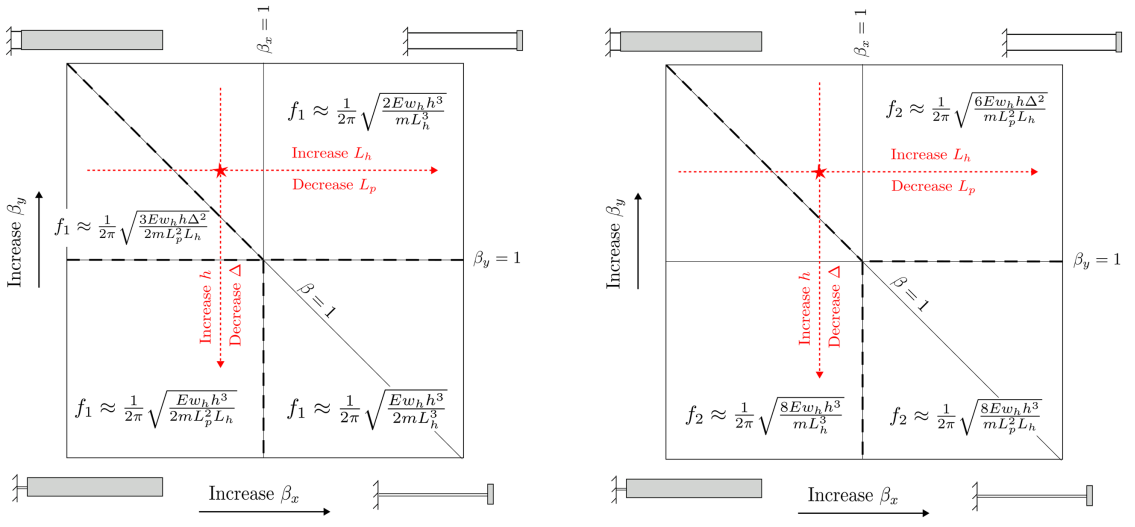

Fig. 9 Summary of frequency terms for a) mode 1 and b) mode 2. The dashed lines indicate the transition boundaries. The red star indicates the point design case in Fig. 6.

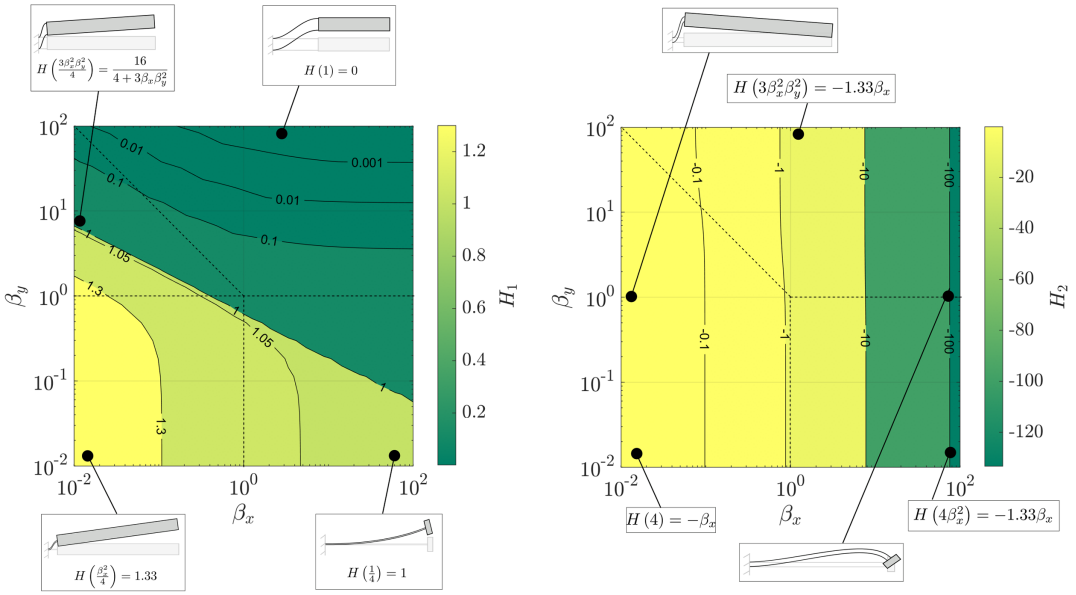

Fig. 10 H_i **as a function of** β_x **and** β_y **for a)** $i = 1$ **and b)** $i = 2$ **with illustrations of expected deformations.**

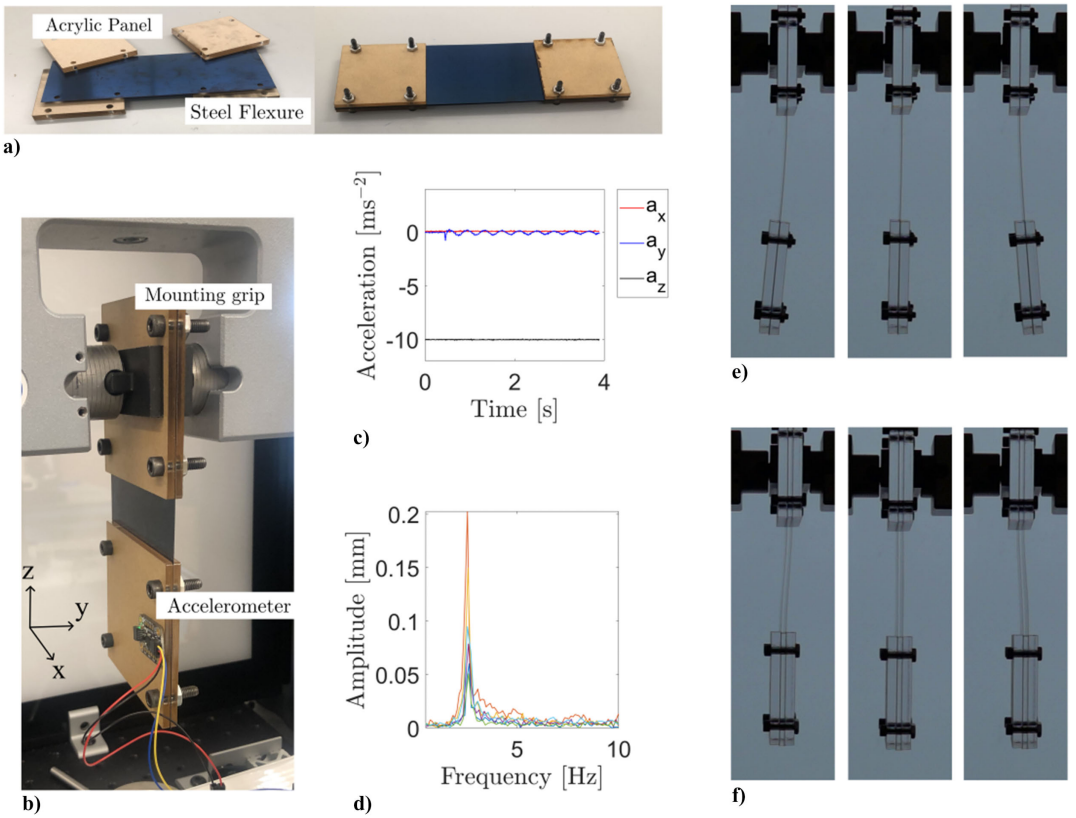

Fig. 11 a) Prototype fabrication and b) the experimental setup; c) a sample case of the recorded acceleration; d) natural frequencies identified through FFT; examples of e) bending- and f) shear-dominated modes.

stowed and deployed without plastic deformation; they are only representative of the deployed configuration.

The prototype is mounted vertically by the top panel; see Fig. 11b, and a three-axis ADXL345 accelerometer (2g range, 230400 baud rate) is attached to the bottom panel. The bottom panel is lightly excited by tapping with an impact hammer and the acceleration profiles are recorded; see Fig. 11c. A fast Fourier transform is applied to the out-of-plane (y) acceleration profile to identify the natural frequencies; see Fig. 11d. A minimum of six tests are averaged for each geometry. Varying the geometry of the flexures and the panel allows us to explore both bending-dominated and shear-dominated modes; see Figs. 11e and 11f.

B. Finite Element Modeling

Here, we carry out two types of finite element simulations, both of them using the commercial software package ABAQUS/Standard.

First, we consider a 2-D model that replicates the same assumptions used in our analytical formulation, including plane strain. Four-node plane strain elements (CPE4) are used for both hinge and panel; see Fig. 12. A modal analysis is carried out for small deflections. The

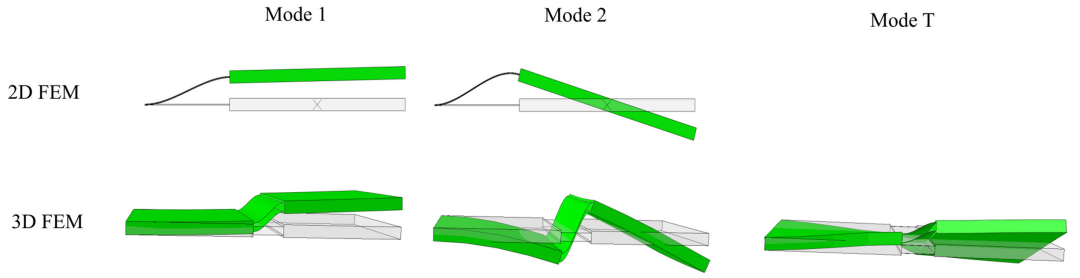

Fig. 12 Primary deformation modes from 2-D and 3-D finite element models.

deformation of the panel is suppressed by defining a rigid body constraint. The hinge is fixed at one edge and connected to the panel using tie constraints with rotational degrees fixed. The inertia of the system accounts for both panel mass and the hinge mass, whereas the analytic model neglects the latter contribution.

We have also conducted simulations with a higher-fidelity three-dimensional (3-D) model, which will be used to identify possible phenomena present in the experiments that cannot be captured by the assumptions of our analytical formulation. Solid elements (C3D8R) are used for the panel and plane stress shells (S4R) for the flexures. Solid-to-shell coupling is defined at the shell–solid intersection, while one panel edge is fixed to prevent rigid body motions. In this case, we do not define a rigid body constraint on the panel and use realistic material properties shown in Table 1. This model shows out-of-plane torsional modes in addition to the in-plane modes from the 2-D analysis, as well as deformation of the acrylic; see Fig. 12.

C. Results

1. *Validating the Analytic Model*

We compare the analytic model against the 2-D finite element model for a total of 400 different configurations on the $\beta_x - \beta_y$ parameter space. The dimensions $L_h = 100$ mm, $h = 0.1$ mm, and $W_h = 1$ mm are fixed while $\Delta = [0.001\text{–}10]$ mm and $L_p = [1\text{–}10,000]$ mm are varied to sweep the $\beta_x - \beta_y$ space in four orders of magnitude. We set the material property to $E_0 = 1 \times 10^7$ MPa and $\nu = 0.3$ to limit the minimum frequency in the order of 0.01 Hz. The same plane strain condition is imposed on the analytic model by using the effective stiffness $E = (E_0/1 - \nu^2)$. The mass of the panel is set at 100 g and mass of the hinge is set at 0.1 g in the finite element method (FEM). The panel thickness in the FEM is set to be 12 mm, while the analytic model assumes the panel to be infinitely thin.

Table 1 Material properties for 3-D finite element model

	Spring steel flexures	Acrylic plate
E, GPa	200	3.3
ν	0.29	0.3
ρ, kg m^{-3}	7800	1220

The relative error between the analytic model and FEM is calculated as

$$f_{\text{error}} = \frac{|f_{\text{analytic}} - f_{\text{FEM}}|}{f_{\text{FEM}}} \tag{38}$$

Figure 13 plots the f_{error} contours on the $\beta_x - \beta_y$ space for the first two modes. The first mode shows an excellent agreement for all $\beta_x - \beta_y$ values with less than 1% error for all cases studied. When we consider the second mode, we again observe excellent agreement in the prediction when $\beta_x < 1$, i.e., when the panel length is longer than the hinge. As the panel length decreases, we observe significant deviations between the 2-D FEM and the analytic model. Closer inspections reveal that as the panel length decreases, the inertia of the hinge becomes more relevant. This is apparent in Fig. 13, in which FEM is able to find mode shapes for the hinges with no panel accelerations. At $\beta_y = 0.01$, FEM finds a mode where the point mass rotates without changing its center of mass, and at $\beta_y = 100$, the flexures bend without moving the panel. The analytic model fails to recognize these modes because the hinge inertia is neglected, and only two DOFs are considered for the flexures (rotation and displacement at one end), which neglects any other possible deformation modes (e.g., the sinusoidal deflection typical of higher modes in a cantilever). Nevertheless, the comparison confirms the validity of the analytic model to predict the first resonance frequency for all possible configurations.

2. *Comparison with Experiments*

Next we compare the experimental observations from the steel hinge prototypes against the analytical predictions and 3-D finite element simulations. Note that the 2-D FEM results are not presented here because they agree with the analytic prediction with an accuracy

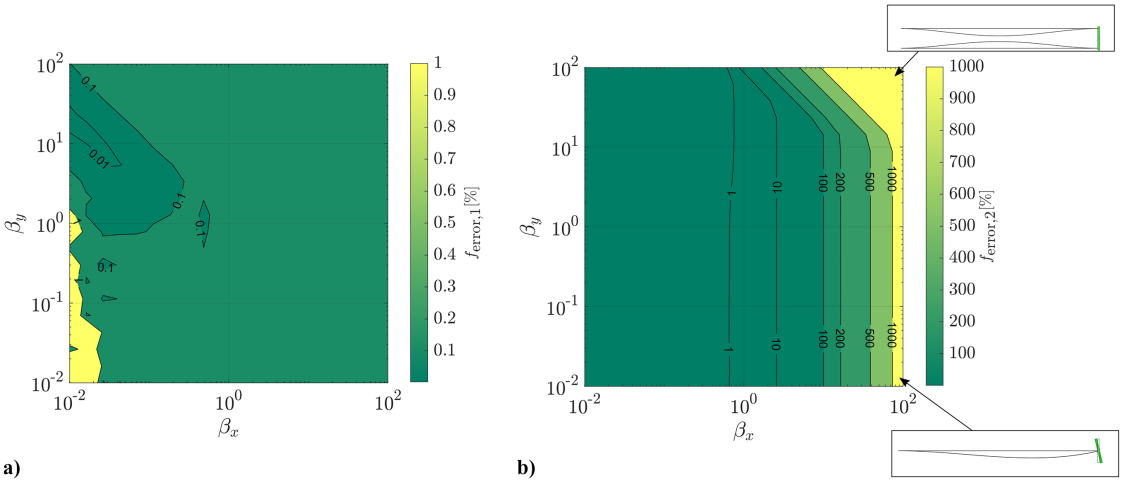

Fig. 13 Contour plot of the relative error f_{error} as a function of $\beta_x - \beta_y$ for a) mode 1 and b) mode 2.

Table 2 Experimental data and natural frequency comparison

Case	L_h, mm	Δ, mm	t_{panel}, mm	m, g	β_x	β_y	β	Analytic, Hz	FEM, Hz	Experiment, Hz	Error[a] %
1	152.4	1.588	7.938	84.05	2.00	12.5	25.00	2.40	2.23	2.58 ± 0.03	7.50
2	127.0	1.588	7.938	84.05	1.67	12.5	20.83	3.14	3.00	3.05 ± 0.07	2.87
3	101.6	1.588	7.938	84.05	1.33	12.5	16.67	4.38	4.22	4.07 ± 0.04	7.08
4	76.2	1.588	7.938	84.05	1.00	12.5	12.50	6.73	6.54	5.90 ± 0.05	12.33
5	50.8	1.588	7.938	84.05	0.67	12.5	8.33	12.28	11.96	9.52 ± 0.06	22.48
6	25.4	1.588	7.938	84.05	0.33	12.5	4.17	33.7	23.2	26.14 ± 0.09	22.43
7	76.2	0.127	6.350	73.55	1.00	1.0	1.00	3.33	3.04	3.59 ± 0.04	7.81
8	76.2	3.175	9.525	116.20	1.00	25.0	25.00	5.32	5.15	5.09 ± 0.04	4.32
9	76.2	6.350	12.70	137.50	1.00	50.0	50.00	5.80	5.62	5.19 ± 0.14	10.52

[a]Error between analytic prediction and experimental observation

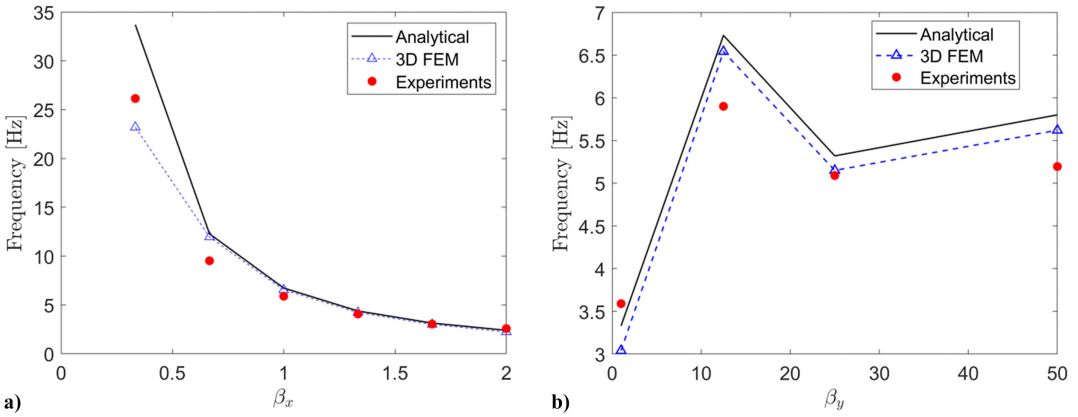

Fig. 14 Comparison of first mode natural frequency between experiments, analytic equation and 3-D FEM as a function of a) β_x (when $\beta_y = 12.5$) and b) β_y (when $\beta_x = 1.0$).

of 0.1% for the selected geometries ($\beta_y \geq 1$). The length parameters are set to the prototype dimensions $h = 0.127$ mm, $W_h = 76.2$ mm, and $L_p = 76.2$ mm. The rest of the parameters for each experiment are shown in Table 2. The mass includes the mass of the acrylic panels, mass of steel that is sandwiched between the acrylic (excluding hinge region), and mass of the tightening bolts. Both models assume the total mass to be uniformly distributed through the panel.

The experimental natural frequencies are described with the average and standard deviation of all tests of the same geometry. The variations between tests are negligible, with standard deviation in the order of 0.1 Hz. Figure 14a visualizes the experimental observations and analytic and FEM predictions as a function of β_x when $\beta_y = 12.5$. In this case, all other parameters are kept constant; hence, the frequency change is dependent only on the length of the hinge. The three cases with $\beta_x > 1$ all have an excellent agreement. However, as the hinge length is shortened, analytic values tend to overpredict the natural frequency. Both FEM and experiments are closer, which can be explained by effects not captured through our analytical formulation, such as the bending of the acrylic panel. As a further source of possible error, the FEM assumes the acrylic panel to be one solid block, whereas in reality, it is composed of several thinner layers sandwiching metal flexures. Next, Fig. 14b compares the frequencies as a function of β_y for constant $\beta_x = 1$. In this case, Δ is increased by adding a thicker acrylic core, which increases the panel mass and explains the non-monotonic evolution of the frequency. We observe a good agreement between the experiments and the numerical predictions.

V. Extension to Other Geometries

The parametric study revealed the existence of clear regions in the $\beta_x - \beta_y$ plane corresponding to different excitation modes for the flat flexure. In this section, we illustrate how this model can be extended to an arbitrary geometry by considering an equivalent flat flexure with the same stiffness.

Let us consider a tape-spring flexure geometry with constant radius R, thickness t, and subtended angle φ. The bending and axial stiffness are estimated as [36]

$$D = \frac{Et\varphi R^3}{2}\left(1 + \frac{\sin(\varphi)}{\varphi} - 2\frac{\sin^2(\varphi/2)}{(\varphi/2)^2}\right) \tag{39}$$

$$A = ER\varphi t \tag{40}$$

We consider two hinge architectures: case A, when the two tape-springs are facing each other, and case B, when facing the opposite direction, as shown in Fig. 15a. Here we assume the horizontal region of each tape-spring is fixed at a distance a_1 and a_2 from each other for case A and B, respectively. Conversely, a different study can be carried out in which the tape-spring distance also changes. For the current study, we can calculate $\Delta = a_i \pm 2y_c$. Here y_c describes the position of the neutral axis of the tape-spring and is given by

$$y_c = R\left(1 - \frac{\sin(\varphi/2)}{(\varphi/2)}\right) \tag{41}$$

The natural frequencies of the tape-spring hinge can be estimated by substituting the stiffness A, D and Δ in Eq. (16). Furthermore, we can extend the parametric investigation in Sec. III by finding an equivalent flat flexure geometry of width $W_{h'}$ and thickness h' that has the same bending and shear stiffness. Using Eq. (17), we obtain

$$h' = R\sqrt{6\left(1 + \frac{\sin(\varphi)}{\varphi} - 2\frac{\sin^2(\varphi/2)}{(\varphi/2)^2}\right)} \tag{42}$$

$$W_{h'} = \frac{\varphi t}{\sqrt{6(1 + (\sin(\varphi)/\varphi) - 2(\sin^2(\varphi/2)/(\varphi/2)^2))}} \tag{43}$$

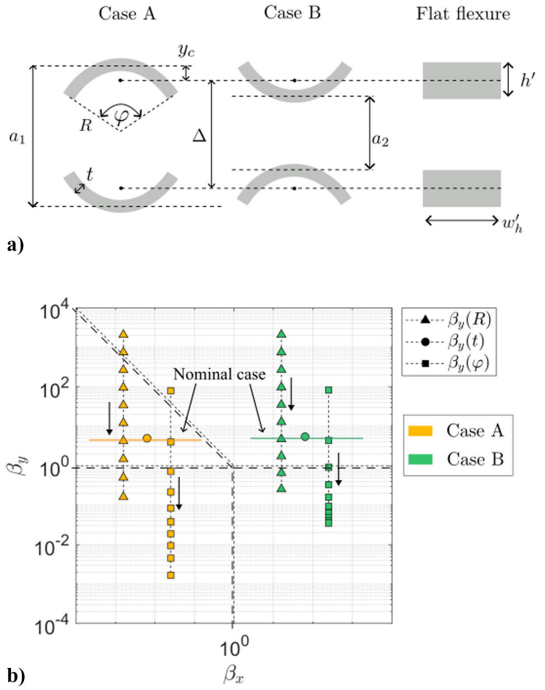

Fig. 15 a) Two possible configurations of tape-spring hinge and the equivalent flat flexure profile; b) dependence of β_y on parameters R, t and φ.

Now we can study the influence of the tape-spring geometry on the modal behavior, which takes place only as part of the β_y parameter:

$$\beta_y(R,\varphi,t) = \frac{a_i \pm R(1-(\sin(\varphi/2)/(\varphi/2)))}{\sqrt{6(1+(\sin(\varphi)/\varphi)-2(\sin^2(\varphi/2)/(\varphi/2)^2))}} \quad (44)$$

We consider a point design of $R_0 = 20$ mm, $t_0 = 1$ mm, $a_{i0} = 40$ mm, and $\varphi_0 = 60$ deg and modify the tape-spring geometry by individually varying $R = [1\text{–}100]$ mm, $t = [0.001\text{–}10]$ mm, and $\varphi = [30\text{–}330]$ degrees. Figure 15b visualizes the dependencies on β_y for each geometric parameter for the two separate cases. The arrows indicate the direction in which the geometric parameter is increased. The geometry of the tape-spring does not affect the β_x, so different β_x values are plotted for each case for visualization clarity.

We observe that β_y of the tape-spring hinge decreases when increasing R and φ, while unaffected by the thickness t. The natural frequencies and parameter dependencies for each $\beta_x - \beta_y$ region can be estimated using the properties of the equivalent cross section, h' and $W_{h'}$, using the understanding of the system summarized in Fig. 9. For example, tape-spring thickness only appears in $W_{h'}$ and affects the natural frequency as $f \propto \sqrt{W_{h'}} \propto \sqrt{t}$.

The preceding analysis is specific for the case of two tape-springs that are kept at a constant gap a_1 and a_2. A similar analysis can be carried out when the flexure positions are also changed or for other cross-sectional geometries. Furthermore, the same approach can be used for systems deploying masses different from the homogeneous panel considered in our study. In this case, it would be necessary to find a panel with equivalent inertia properties to those of the deployed mass.

VI. Conclusions

This paper has studied the free vibration dynamics of a flexible hinge with shear compliance attached to a rigid panel. We idealize the structure as a two-degree-of-freedom 2-D system and account for both bending and shear stiffness in the hinge by modeling it as a Timoshenko beam. We provide a closed-form solution for both natural frequency and vibration modes and specialize the solution for the case of a hinge composed by two flat flexures. We identify two length scales, β_x and β_y, that control the dynamics of the system. This parameterization allows us to divide the design space into regions with distinct response and understand the influence of each parameter on both the natural frequency and the vibration modes. The accuracy of our formulation was confirmed through comparisons with a 2-D finite element model, with less than 1% difference in the prediction of the first natural frequency. For the second mode, the hinge inertia becomes significant for $\beta_x > 1$, which is not captured in the analytic model. We have also performed experiments with prototypes of different geometries, with good agreement with our model. Some of the differences can be explained as due to the finite stiffness of the panel, which is observed in high-fidelity 3-D finite element simulations.

Our formulation provides not only a closed-form estimate for the first natural frequency but also insight into how the properties of the system drive the interplay between bending and shearing modes commonly observed in elastically folding deployable elements. Particularly interesting for new designs, it explains which change in parameters will have the larger effect on a given geometry. For example, it is possible to identify at which point increasing the flexure separation does not increase the natural frequency, due to the appearance of shearing modes, as a function of the other system parameters. Furthermore, we have shown that the framework can be easily extended to curved geometries, with an example case of tape-spring–based hinges.

The results presented in this paper will play a key role in enabling the design of flexure-based hinges for deployable structures, yet some questions remain open. First, the geometry of the flexures needs to allow folding so that the structure can act as a hinge. This results in a new set of requirements that often drive the design in the opposite direction from those derived from modal analysis (e.g., long flexures make the hinge easier to fold but reduce the natural frequency). The authors are currently working on a manuscript addressing this aspect of the design. Second, the model has not considered torsional modes, the inertia of the hinge, or the stiffness of the panel. The three-dimensional simulations and the experiments show that, in some cases, these idealizations have a significant effect. Finally, we plan to extend our work to the case of a structure deploying several panels, either in an accordion-like architecture or through more complex connectivity.

Acknowledgments

The University of Colorado Boulder team thanks JPL Strategic University Research Partnership for funding this project. Part of the research was carried out at the Jet Propulsion Laboratory, California Institute of Technology, under a contract with the National Aeronautics and Space Administration (80NM0018D0004).

References

[1] Miura, K., "Concepts of Deployable Space Structures," *International Journal of Space Structures*, Vol. 8, Nos. 1–2, 1993, pp. 3–16. https://doi.org/10.1177/0266351193008001-202

[2] Santoni, F., Piergentili, F., Donati, S., Perelli, M., Negri, A., and Marino, M., "An Innovative Deployable Solar Panel System for Cubesats," *Acta Astronautica*, Vol. 95, Feb. 2014, pp. 210–217. https://doi.org/10.1016/j.actaastro.2013.11.011

[3] Hodges, R. E., Chahat, N. E., Hoppe, D. J., and Vacchione, J. D., "The Mars Cube One Deployable High Gain Antenna," *2016 IEEE International Symposium on Antennas and Propagation (APSURSI)*, IEEE Publ., Piscataway, NJ, 2016, pp. 1533–1534. https://doi.org/10.1109/APS.2016.7696473

[4] Sauder, J. F., Arya, M., Chahat, N., Thiel, E., Dunphy, S., Shi, M., Agnes, G., and Cwik, T., "Deployment Mechanisms for High Packing Efficiency One-Meter Reflectarray Antenna (OMERA)," *AIAA Scitech 2019 Forum*, AIAA Paper 2019-0755, 2019. https://doi.org/10.2514/6.2019-0755

[5] Sols-Santomé, A., Urriolagoitia-Sosa, G., Romero-Ángeles, B., Torres-San Miguel, C. R., Hernández-Gómez, J. J., Medina-Sánchez, I., Couder-Castañeda, C., Grageda-Arellano, J. I., and Urriolagoitia-Calderón, G., "Conceptual Design and Finite Element Method Validation of a New Type of Self-Locking Hinge for Deployable CubeSat Solar Panels," *Advances in Mechanical Engineering*, Vol. 11, No. 1, 2019. https://doi.org/10.1177/1687814018823116

[6] Fernandez, J. M., "Advanced Deployable Shell-Based Composite Booms for Small Satellite Structural Applications Including Solar Sails," *International Symposium on Solar Sailing 2017*, Japan Space Forum, 2017, NF1676L-25486.

[7] Adams, D. S., and Mobrem, M., "Lenticular Jointed Antenna Deployment Anomaly and Resolution Onboard the Mars Express Spacecraft," *Journal of Spacecraft and Rockets*, Vol. 46, No. 2, 2009, pp. 403–410. https://doi.org/10.2514/1.36891

[8] Mallikarachchi, H., and Pellegrino, S., "Quasi-Static Folding and Deployment of Ultrathin Composite Tape-Spring Hinges," *Journal of Spacecraft and Rockets*, Vol. 48, No. 1, 2011, pp. 187–198. https://doi.org/10.2514/1.47321

[9] Sicre, J., Givois, D., and Emerit, A., "Application of 'Maeva' Hinge to Myriade Microsatellites Deployments Needs," *Proceedings of the 11th European Space Mechanisms and Tribology Symposium, ESMATS 2005*, Vol. 591, edited by B. Warmbein, ESA SP-591, European Space Agency Publications Division, Noordwijk, The Netherlands, 2005, pp. 243–250.

[10] Silver, M., and Echter, M., "Precision High-Strain Composite Hinges for Deployable Space Telescopes," *44th Aerospace Mechanisms Symposium*, Vol. 417, Mechanisms Education Assoc., 2018.

[11] Feria, V., Lou, M., Huang, J., and Speer, S., "Lightweight Deployable Space Radar Arrays," *39th AIAA/ASME/ASCE/AHS/ASC Structures, Structural Dynamics, and Materials Conference and Exhibit*, AIAA Paper 1998-1933, 1998. https://doi.org/10.2514/6.1998-1933

[12] Soykasap, Ö., "Analysis of Tape Spring Hinges," *International Journal of Mechanical Sciences*, Vol. 49, No. 7, 2007, pp. 853–860. https://doi.org/10.1016/j.ijmecsci.2006.11.013

[13] Echter, M. A., Gillmer, S. R., Silver, M. J., Reid, B. M., and Martinez, R. E., "A Multifunctional High Strain Composite (HSC) Hinge for Deployable In-Space Optomechanics," *Smart Materials and Structures*, Vol. 29, No. 10, 2020, Paper 105010. https://doi.org/10.1088/1361-665X/abad4d

[14] Mierheim, O., Glaser, T., Hobbie, C. F., Kottmeier, S., and Hühne, C., "The Tape Spring Hinge Deployment System of the Eu: CROPIS Solar Panels," *European Conference on Spacecraft Structures, Materials and Mechanical Testing, Proceedings*, European Space Agency, 2018.

[15] Dharmadasa, B. Y., Lopez Jimenez, F., Arya, M., Mejia-Ariza, J., Sauder, J. F., Focardi, P., and Bradford, S. C., "Design and Fabrication of a High Strain Composite Flexure for CubeSat Reflect Arrays," *AIAA SCITECH 2022 Forum*, AIAA Paper 2023-0581, 2023. https://doi.org/10.2514/6.2023-0581

[16] Ziade, E., Patmont, C. S., and Fritz, T. A., "Design and Characterization of a Spring Steel Hinge for Deployable CubeSat Structures," *Journal of Small Satellites*, Vol. 5, No. 1, 2016, pp. 407–418.

[17] Lan, X., Liu, L., Pan, C., Li, F., Liu, Z., Hou, G., Sun, J., Dai, W., Wang, L., Yue, H., Liu, Y., and Leng, J., "Smart Solar Array Consisting of Shape-Memory Releasing Mechanisms and Deployable Hinges," *AIAA Journal*, Vol. 59, No. 6, 2021, pp. 2200–2213. https://doi.org/10.2514/1.J059281

[18] Dao, T. D., Ha, N. S., Goo, N. S., and Yu, W.-R., "Design, Fabrication, and Bending Test of Shape Memory Polymer Composite Hinges for Space Deployable Structures," *Journal of Intelligent Material Systems and Structures*, Vol. 29, No. 8, 2018, pp. 1560–1574. https://doi.org/10.1177/1045389X17742728

[19] Sakovsky, M., and Pellegrino, S., "Closed Cross-Section Dual-Matrix Composite Hinge for Deployable Structures," *Composite Structures*, Vol. 208, Jan. 2019, pp. 784–795. https://doi.org/10.1016/j.compstruct.2018.10.040

[20] Hedgepeth, J., "Critical Requirements for the Design of Large Space Structures," *2nd Conference on Large Space Platforms: Toward Permanent Manned Occupancy in Space*, AIAA Paper 1981-0443, 1981. https://doi.org/10.2514/6.1981-443

[21] Seffen, K., and Pellegrino, S., "Deployment Dynamics of Tape Springs," *Proceedings of the Royal Society of London. Series A: Mathematical, Physical and Engineering Sciences*, Vol. 455, No. 1983, 1999, pp. 1003–1048. https://doi.org/10.1098/rspa.1999.0347

[22] Walker, S. J., and Aglietti, G., "Study of the Dynamics of Three Dimensional Tape Spring Folds," *AIAA Journal*, Vol. 42, No. 4, 2004, pp. 850–856. https://doi.org/10.2514/1.908

[23] Mobrem, M., and Adams, D. S., "Deployment Analysis of the Lenticular Jointed Antennas Onboard the Mars Express Spacecraft," *Journal of Spacecraft and Rockets*, Vol. 46, No. 2, 2009, pp. 394–402. https://doi.org/10.2514/1.42496

[24] Kwok, K., and Pellegrino, S., "Folding, Stowage, and Deployment of Viscoelastic Tape Springs," *AIAA Journal*, Vol. 51, No. 8, 2013, pp. 1908–1918. https://doi.org/10.2514/1.J052269

[25] Mallikarachchi, H., and Pellegrino, S., "Deployment Dynamics of Ultrathin Composite Booms with Tape-Spring Hinges," *Journal of Spacecraft and Rockets*, Vol. 51, No. 2, 2014, pp. 604–613. https://doi.org/10.2514/1.A32401

[26] Kim, K.-W., and Park, Y., "Systematic Design of Tape Spring Hinges for Solar Array by Optimization Method Considering Deployment Performances," *Aerospace Science and Technology*, Vol. 46, Oct. 2015, pp. 124–136. https://doi.org/10.1016/j.ast.2015.06.013

[27] Aridon, G., Blanchard, L., Remond, D., and Dufour, R., "Modal Identification for Modeling a Deployed Tape-Spring Hexapod," *47th AIAA/ASME/ASCE/AHS/ASC Structures, Structural Dynamics, and Materials Conference 14th AIAA/ASME/AHS Adaptive Structures Conference 7th*, AIAA Paper 2006-1977, 2006. https://doi.org/10.2514/6.2006-1977

[28] Soykasap, Ö., Pellegrino, S., Howard, P., and Notter, M., "Folding Large Antenna Tape Spring," *Journal of Spacecraft and Rockets*, Vol. 45, No. 3, 2008, pp. 560–567. https://doi.org/10.2514/1.28421

[29] Oberst, S., Tuttle, S., Griffin, D., Lambert, A., and Boyce, R., "Experimental Validation of Tape Springs to be Used as Thin-Walled Space Structures," *Journal of Sound and Vibration*, Vol. 419, April 2018, pp. 558–570.

[30] Lakshmi, S. S., Varsha, M., Krishnaa, G. S., Kuriakose, V. M., Subhani, S. M., Subramanian, H. S., and Sreehari, V., "Thermo-Structural Analysis of Deployable Composite Booms with Slotted Hinges for Space Applications," *Materials Today: Proceedings*, Vol. 56, Jan. 2022, pp. 3564–3570. https://doi.org/10.1016/j.matpr.2021.11.633

[31] Fernandes, P., Pinto, R., Ferrer, A., and Correia, N., "Performance Analysis of a Damage Tolerant Composite Self-Deployable Elastic-Hinge," *Composite Structures*, Vol. 288, May 2022, Paper 115407. https://doi.org/10.1016/j.compstruct.2022.115407

[32] Rose, T., Hensley, W. B., and Francis, W., "Solid-State Hinge Mechanism for Simple Panel Deployment System," *45th Aerospace Mechanisms Symposium*, NASA Johnson Space Center, Mechanisms Education Assoc., Tujunga, CA, 2020.

[33] Yorgiadis, A., and Barrett, S., "Flexure Guides for Vibration Testing," *39th Symposium on Shock and Vibration*, Shock and Vibration Information Center, Naval Research Lab., Washington, D.C., 1968, pp. 157–174.

[34] Smith, S. T., *Flexures: Elements of Elastic Mechanisms*, CRC Press, Boca Raton, FL, 2000. https://doi.org/10.1201/9781482282962

[35] Timoshenko, S. P., "On the Transverse Vibrations of Bars of Uniform Cross-Section," *London, Edinburgh, and Dublin Philosophical Magazine and Journal of Science*, Vol. 43, No. 253, 1922, pp. 125–131. https://doi.org/10.1080/14786442208633855

[36] Yang, Y., Qin, Y., Tang, Y., Yang, Y., Peng, Y., and Pu, H., "Deployable Closed-Loop Tape-Spring Manipulators with Mobile Drive Components on Localized Folds," *Mechanism and Machine Theory*, Vol. 167, Jan. 2022, Paper 104553. https://doi.org/10.1016/j.mechmachtheory.2021.104553

R. K. Kapania
Associate Editor